

Dynamic versus quasi-static response of a cantilevered beam rotated harmonically

Gilad Yakir, Eduardo Gutierrez-Prieto, and Pedro M. Reis
*Flexible Structures Laboratory, Institute of Mechanical Engineering,
École Polytechnique Fédérale de Lausanne (EPFL), 1015 Lausanne, Switzerland*

We investigate a cantilevered elastic beam subjected to harmonic rotational motion. In the rotating frame, the beam experiences centrifugal and Euler fictitious forces, with negligible Coriolis effects. We validate a reduced-order *elastica* model through precision experiments on slender beams rotating with a controlled sinusoidal angular velocity. Systematically exploring the parameter space, we identify regimes where inertial effects are negligible, enabling a quasi-static treatment despite harmonic driving. We characterize the transition to dynamic response using two dimensionless parameters, the Euler and centrifugal numbers, which compare centrifugal and Euler forces to bending forces. Counterintuitively, the quasi-static regime expands as rotational speed increases: faster rotation produces less dynamic response. The critical Euler number separating these regimes remains constant at low centrifugal numbers but follows square-root scaling at higher rotation rates, a transition driven by centrifugal stiffening. Our results establish the conditions under which quasi-static approximations remain valid for rotating flexible beams under harmonic driving.

I. INTRODUCTION

Nearly every machine built since the Industrial Revolution involves rotating components [28], including wheels, gears, fans, and turbines. These components have become so ubiquitous that they often go unnoticed. Regardless of their size and purpose, the dynamics of rotating systems is described by a set of differential equations in a frame of reference (FoR) [23], which can be either inertial or non-inertial. Analyzed in a non-inertial frame, rotating systems are governed by three fictitious forces: *centrifugal*, *Euler*, and *Coriolis* forces. The *centrifugal force* scales with the square of angular velocity and acts radially outward. The *Euler force* acts tangentially, opposite to angular acceleration, and arises from changes in angular velocity. The *Coriolis force* acts perpendicular to both the angular velocity and the relative velocity. Although there is substantial literature on the structural response of rotating beams under steady rotation [2, 8, 10, 20, 30, 33, 34], relatively few studies have examined systems with unsteady angular velocities where Euler forces become important.

The effect of fictitious forces on point masses is well-established and commonly taught in introductory *Dynamics* courses. However, their influence is more nuanced for rotating structures, where these forces interact with the body's geometric and material properties to dictate the mechanical response. Early foundational work on rotating beams and shafts was pioneered by Rankine and Jeffcott [17, 26]; the latter's work, in particular, is often regarded as the first fundamental theory of rotor-dynamics.

Rotation critically affects the vibration characteristics of rotating beams [15, 37]; centrifugal forces cause stretching, which increases the bending stiffness and shifts natural frequencies and mode shapes [5, 36, 37]. When rotational acceleration is considered, the Euler force induces tangential deformation, introducing

acceleration-dependent coupling in the governing beam equations [19]. Recent work by [9] further demonstrated these effects for a pitching cantilever beam subjected to both constant and time-varying angular velocities, showing that incorporating Euler forces significantly affects the beam's dynamic response. Notably, linearized geometric approximations become inadequate in this regime, failing to accurately predict both the bending deflection amplitude and the twist angle. This underscores the need to account for Euler forces in rotating structures.

We previously investigated rotating cantilevered and bistable beams under constant angular acceleration, characterized by linear velocity profiles, focusing on the resulting buckling behavior [13]. For a cantilever beam clamped radially with the free end pointing to the center of rotation, the results revealed a critical interplay between the beam's natural curvature and the applied Euler force in dictating the buckling direction. For a bistable beam, on-demand snap-through transitions could be induced by Euler forces, enabling controlled switching between stable states. We later demonstrated that dynamic driving protocols enable independent control of bistable elements for programmable mechanical memory [14]. Despite these contributions, significant knowledge gaps remain in understanding how velocity-dependent centrifugal forces interact with acceleration-dependent Euler forces under time-varying conditions. While prior studies have typically focused on steady or simplified rotational profiles, few have systematically explored the transition between dynamic and quasi-static responses in harmonically rotated cantilever beams or revealed how intrinsic mechanics suppress inertial effects under unsteady conditions.

Here, we assess the validity of a quasi-static approximation for unsteadily rotated cantilever beams. Quasi-static approximations offer significant computational advantages and are preferred in engineering analysis [1, 6, 25, 29]. However, the validity conditions of this approximation for rotating structures remain largely unex-

pored. We adopt an existing reduced-order model based on Euler's *elastica* in a rotating frame [13] and validate it against precision experiments. We identify a regime where the beam's response can be accurately predicted by assuming quasi-static behavior under instantaneous forcing. These results highlight the interplay between centrifugal and Euler forces, establishing when simplified models are suitable for analyzing and designing rotating elastic systems. We then systematically explore material and geometric parameters, enabling us to perform a theoretical analysis that predicts the transition between quasi-static and dynamic behavior in slender rotating beams.

Our manuscript is structured as follows. Section II defines the system and outlines the research questions. Sections III and IV revisits the reduced-order rotating *elastica* model from [13] and describes its implementation, while Section V presents the experimental apparatus and protocols. We validate the numerical model against experiments in Section VI, then define the quasi-static-to-dynamic boundary and identify where quasi-static assumptions are valid in Section VII. Section VIII derives a theoretical description of the boundary, showing that centrifugal stiffening governs this transition. Finally, Section IX concludes and suggests future directions.

II. PROBLEM DEFINITION

We investigate the elastic deformation of a cantilevered beam mounted on an unsteadily rotating FoR, as shown schematically in Fig. 1(a). Our system is similar to that of [13]. A rotating triad (\mathbf{e}_x , \mathbf{e}_y , \mathbf{e}_z) is attached to the center of rotation O . The beam is clamped at a distance R_o from O with its undeformed centerline along $+\mathbf{e}_x$. The FoR is rotated with angular velocity $\Omega(t)$ [rad/s] and angular acceleration $\dot{\Omega}(t) = d\Omega(t)/dt$ [rad/s²] (Fig. 1b-c). The beam has arclength L , rectangular cross-section (thickness h , width b , cross-sectional area $A = bh$, and moment of inertia $I = bh^3/12$), Young's modulus E , and density ρ . We assume the beam is slender ($h = \lambda_1 L$, with $\lambda_1 \ll 1$), inextensible, and unsharable. The cross-section has width $b = \lambda_2 h$, with $\lambda_2 > 1$, and deformations are purely in-plane ($z = 0$). Using standard *elastica* kinematics, the centerline is parameterized by $s \in [0, L]$, from the clamp ($s = 0$) to the free end ($s = L$), with position $\mathbf{r}(s, t) = x(s, t)\mathbf{e}_x + y(s, t)\mathbf{e}_y$ and tangent angle $\theta(s, t)$ relative to \mathbf{e}_x defined by $\partial\mathbf{r}/\partial s = \mathbf{r}_{,s} = \cos\theta\mathbf{e}_x + \sin\theta\mathbf{e}_y$. The Cartesian coordinates of the centerline at s are

$$\begin{aligned} x(s) &= \int_0^s \cos\theta(s')ds' \quad \text{and} \\ y(s) &= \int_0^s \sin\theta(s')ds'. \end{aligned} \quad (1)$$

The rotating beam experiences three *fictitious* body

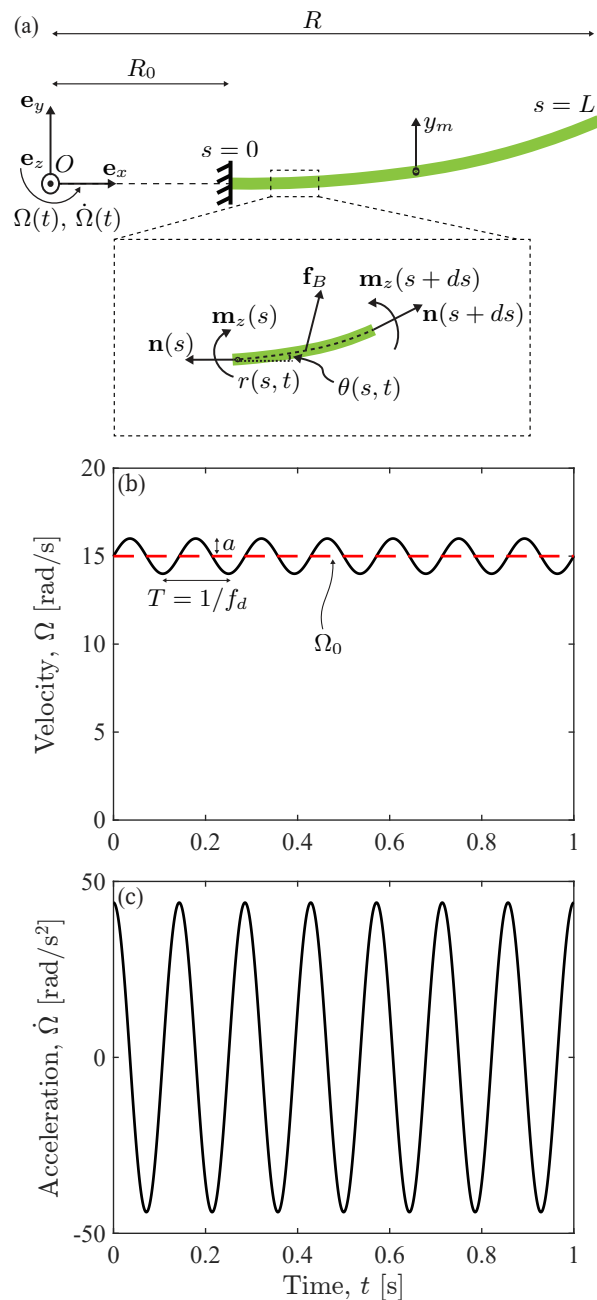


FIG. 1. Schematic of a rotating cantilevered beam. (a) The slender beam (arclength L) is clamped at a distance R_o from the center of rotation, O , with the system rotating about \mathbf{e}_z at angular velocity $\Omega(t)$ and acceleration $\dot{\Omega}(t)$. Inset: Infinitesimal beam element at arclength s showing fictitious body force $\mathbf{f}_B = \mathbf{f}_c + \mathbf{f}_w + \mathbf{f}_e$; cf. Eqs. (2-4), internal tension \mathbf{n} and moment \mathbf{m}_z . (b) Representative sinusoidal angular velocity profile $\Omega(t)$ with mean $\Omega_0 = 15$ rad/s, amplitude $a = 1$ rad/s, and frequency $f_d = 7$ Hz. (c) Corresponding angular acceleration $\dot{\Omega}$.

loads, the Coriolis, centrifugal, and Euler forces:

$$\mathbf{f}_c(t) = -2\rho A\Omega\mathbf{e}_z \times \dot{\mathbf{r}}, \quad (2)$$

$$\mathbf{f}_\omega(t) = \rho A\Omega^2\mathbf{r}, \quad (3)$$

$$\mathbf{f}_e(t) = -\rho A\dot{\Omega}\mathbf{e}_z \times \mathbf{r}. \quad (4)$$

[13] previously studied a rotating cantilevered beam under constant angular acceleration, oriented to apply a compressive centrifugal force. This induced a buckling instability whose direction could be tuned via the Euler force. Here, we reverse the beam's orientation, making the centrifugal force tensile, and impose a *harmonic* rather than a constant angular velocity. Despite this dynamic loading, we demonstrate that, under certain conditions, the system behaves quasi-statically. Our goal is to characterize the boundary where the quasi-static approximation breaks down.

We impose sinusoidal angular velocity profiles,

$$\Omega(t) = a \sin(2\pi f_d t) + \Omega_0, \quad (5)$$

with corresponding angular acceleration

$$\dot{\Omega}(t) = 2\pi a f_d \cos(2\pi f_d t), \quad (6)$$

where a is the amplitude, f_d the drive frequency, and Ω_0 the mean angular velocity. Representative profiles are shown in Fig. 1(b, c).

Due to the beam's size and velocity, the Coriolis force \mathbf{f}_c is negligible compared to centrifugal and Euler forces. Following [13], the ratio $|\mathbf{f}_c|/|\mathbf{f}_\omega| \sim |(\dot{\mathbf{r}})_r|/(\Omega R)$ indicates that \mathbf{f}_c is significant only when the beam's velocity in the FoR is comparable to the tangential velocity of the imposed rotation, which does not occur for the parameters we explore.

With Coriolis forces neglected, the driving profiles in Eqs. (5) and (6) control the relative effects of centrifugal and Euler forces by tuning the mean angular velocity Ω_0 relative to the angular acceleration amplitude, $\alpha = 2\pi a f_d$. Unlike constant acceleration, harmonic driving allows the beam to reach a steady-state oscillatory response. We fix the velocity amplitude at $a = 1$ rad/s, so that varying the drive frequency f_d independently controls the angular acceleration magnitude $\alpha = 2\pi f_d$. This allows us to discern the relative influence of the Euler and centrifugal forces.

We apply the theoretical framework from [13] to perform numerical simulations validated against precision experiments. We identify regions in parameter space where the beam's response is either *dynamic* (when inertial effects are significant) or *quasi-static* (when instantaneous static forces accurately predict the response). We will demonstrate that quasi-static conditions occur under large centrifugal loadings; counterintuitively, faster rotation leads to less dynamic response.

In summary, we aim to answer two key questions: (i) When can a harmonically rotating structure produce a quasi-static response? (ii) When do inertial effects become significant enough to shift the behavior from quasi-static to dynamic?

III. THEORETICAL FORMULATION

We adopt the *elastica*-based model developed by [13] for a thin, linear-elastic cantilevered beam in a rotating frame. For completeness, we briefly review this model, derived from force and moment balance on an infinitesimal element of the beam (see schematic in the inset of Fig. 1a). The dimensional equations are nondimensionalized using the total arclength L for length, the characteristic bending force EI/L^2 for forces, and the bending frequency scale $f_s = (2\pi)^{-1}\sqrt{EI/\rho AL^4}$ for time. (Hereafter, overdots denote time derivatives $\dot{b}(t) = \partial b/\partial t$ for dimensional time and $\dot{\tilde{b}}(\tau) = \partial \tilde{b}/\partial \tau$ for dimensionless quantities.) The first natural frequency of the beam is

$$f_n = \beta_1^2 f_s = \frac{\beta_1^2}{2\pi} \sqrt{\frac{EI}{\rho AL^4}}, \quad (7)$$

where $\beta_1 = 1.875$ is the modal constant for the first mode [22]. The resulting dimensionless equations of motion are

$$\mathbf{e}_x : n_{x,s} + 2\mathcal{I}\dot{y} + \mathcal{C}(1 - \delta + \delta x) + \quad (8)$$

$$\delta\mathcal{E}y = \ddot{x} + \eta\dot{x},$$

$$\mathbf{e}_y : n_{y,s} - 2\mathcal{I}\dot{x} + \mathcal{E}(1 - \delta + \delta x) + \quad (9)$$

$$\delta\mathcal{C}y = \ddot{y} + \eta\dot{y},$$

$$\mathbf{e}_z : \theta_{,ss} - n_x \sin\theta + n_y \cos\theta = 0, \quad (10)$$

where we use the notation $\partial\langle\cdot\rangle/\partial s = \langle\cdot\rangle_{,s}$ and $\partial^2\langle\cdot\rangle/\partial s^2 = \langle\cdot\rangle_{,ss}$ for spatial partial derivatives. The dimensionless quantities are arclength $s \in [0, 1]$, time τ , horizontal x and vertical y displacements, internal tension $\mathbf{n} = n_x \mathbf{e}_x + n_y \mathbf{e}_y$, geometric ratio $\delta = L/R$, and viscous damping coefficient $\eta = \gamma L^2/\sqrt{\rho A EI}$ (in Appendix B, we determine γ , which accounts for internal dissipation effects). The dimensionless centrifugal, Euler, and inertial numbers in Eqs. (8–10) are

$$\mathcal{C}(\tau) = \frac{\rho A R L^3}{EI} \Omega^2(\tau), \quad (11)$$

$$\mathcal{E}(\tau) = \frac{\rho A R L^3}{EI} f_s \dot{\Omega}(\tau), \quad (12)$$

$$\mathcal{I}(\tau) = \frac{\rho A L^4}{EI} f_s \dot{\Omega}(\tau), \quad (13)$$

which quantify the corresponding forces (Eqs. 2-4) relative to the characteristic bending forces per unit length, EI/L^3 .

Assuming zero natural curvature, the boundary conditions for our cantilevered configuration (Fig. 1) are

$$\begin{aligned} x(0, \tau) &= 0, & y(0, \tau) &= 0, \\ n_x(1, \tau) &= 0, & n_y(1, \tau) &= 0, \\ \theta(0, \tau) &= 0, & \theta_{,s}(1, \tau) &= 0. \end{aligned} \quad (14)$$

IV. METHODOLOGY: NUMERICAL SIMULATIONS

While we use the same governing Eqs. (8–10) as [13], several differences require adapting the discretization procedure: our reversed beam orientation produces tensile rather than compressive centrifugal loading (cf. Section II); we impose different boundary conditions (Eq. 14); and we apply harmonic rather than constant driving (Eqs. 5-6). The modified spatial discretization is outlined below and detailed in Appendix A, with key changes in the integration limits (Eq. 1) and discretization matrices \mathbf{L} , \mathbf{U} , and \mathbf{K} .

Discretizing Eqs. (8–10) yields $N-1$ coupled nonlinear ODEs for the tangential angle vector $\Theta = [\theta_1, \dots, \theta_{N-1}]^T$:

$$\mathbf{M}\ddot{\Theta} + \mathbf{C}\dot{\Theta} + \mathbf{K}\Theta = \mathbf{f}, \quad (15)$$

where \mathbf{M} , \mathbf{C} , and \mathbf{K} are the mass, damping, and stiffness matrices, and \mathbf{f} is the forcing vector. All these quantities are defined in Appendix A. After a convergence test (see Appendix C), we use $N=40$ nodes and solve Eq. (15) with MATLAB’s stiff ODE solver `ode23tb`.

Quasi-static solutions are obtained by setting all time derivatives in Eqs. (8–10) to zero, reducing the problem to instantaneous static equilibrium under time-varying forces. We solve these equations with MATLAB’s boundary value problem solver, `bvp4c`. We explore drive parameters in the ranges: $\mathcal{C} \in [0.03, 787]$ and $\mathcal{E} \in [0.2, 44]$.

V. METHODOLOGY: EXPERIMENTS

We validate the numerical model described in Sections III and IV with experiments using the apparatus shown in Fig. 2(a). The setup comprises a torque-controlled motor ① that rotates a rigid disk ② with the cantilevered beam ③ mounted at a distance R_o from the rotation center (O). A camera ⑥ fixed in the lab frame images the beam deformation. The circular disk design balances the motor load, enabling higher velocities and accelerations while reducing high-frequency noise. Figure 2(b) shows a top view of the rotating disk with the clamped beam, while Fig. 2(c) presents representative experimental frames overlaid with the experimentally measured midspan of the beam (magenta diamonds) and simulation predictions (green circles) for driving parameters $\Omega_0 = 15$ rad/s, and $f_d = 7$ Hz. We now describe the apparatus components and protocol in detail.

a. Rotating system Our rotating rigid disk (350 mm diameter and 20 mm thickness) is mounted to a torque-controlled motor (ETEL RTMB1140-150, driver AccurET 600). This motor accurately imposes arbitrary, time-varying velocity and acceleration profiles by using an input look-up table of angular position and time pairs, computed from Eqs. (5–6). An encoder records the angular position of the motor at 20 kHz, providing high-precision velocity and acceleration measurements and

real-time feedback for closed-loop control. The system’s frameless architecture and high torque stability eliminate backlash and vibrations, enabling accurate tracking during dynamic operation.

b. Beam fabrication We cast beam samples from Elite Double 32, a vinyl polysiloxane (VPS) elastomer (Zhermack Dental) [13]. This two-part system is mixed in a 1:1 mass ratio (base to catalyst) and poured into a mold to produce samples of width $b=10$ mm, thickness $h=2$ mm, and length $L=40$ mm. The material cures in 20 minutes, although its mechanical properties stabilize only after about 10 days. Previous studies [3, 12, 18] show that VPS32 behaves as an incompressible Neo-Hookean material, with a Young’s modulus of $E = 1.22 \pm 0.05$ MPa and a Poisson’s ratio of $\nu \approx 0.5$. The beam’s first natural frequency is $f_n = 6.37$ Hz, computed via Eq. (7) with $\beta_1 = 1.875$. The beam parameters are summarized in Table I; in subsequent sections, we refer to this as our *reference beam*.

L [mm]	h [mm]	b [mm]	E [MPa]	ρ [kg/m ³]
40	2	10	1.22	1170.2

TABLE I. Geometric and material properties of the beam studied in Sections V to VII.

c. Beam mounting We clamp the cured beam inside a hollow acrylic disk, as shown in Fig. 2(b). The disk comprises three parts: a central section that securely clamps the beam, and an acrylic top plate and bottom dish that enclose the beam. This enclosure reduces aerodynamic drag during rotation. The entire disk is painted black to enhance optical contrast for image processing.

d. Imaging and image processing We image the beam in the lab frame using a digital camera (*IDS U3-3040SE-M-GL*) mounted 1.15 m above the rotating disk. We process the acquired images using an in-house *Python* algorithm based on the *skimage* library [35]. This algorithm first stabilizes the images in the rotating frame by detecting the two circular markers visible in Fig. 2(b): one fixed at the rotation center (O) and the other rotating at a known radius of 65 mm. After detecting the markers, the algorithm rotates each frame using bi-cubic interpolation to align them. The algorithm then skeletonizes the beam to obtain its centerline. Since skeletonization may introduce artifacts near the beam’s edges, we focus on the vertical deflection at the beam’s midspan (y_m), which is more robust to such errors. A representative series of frames is shown in Fig. 3(b) with the detected midspan locations marked with magenta diamonds.

e. Experimental protocol The beam is mounted onto the rigid rotating acrylic disk and enclosed between the two covers. A command is sent to the motor to rotate the disk at the desired angular velocity and acceleration profile (cf. Eqs. 5-6). A hardware signal from the motor controller triggers image acquisition, which continues throughout the experiment. Both the image and motor data are post-processed, and each experiment is repeated

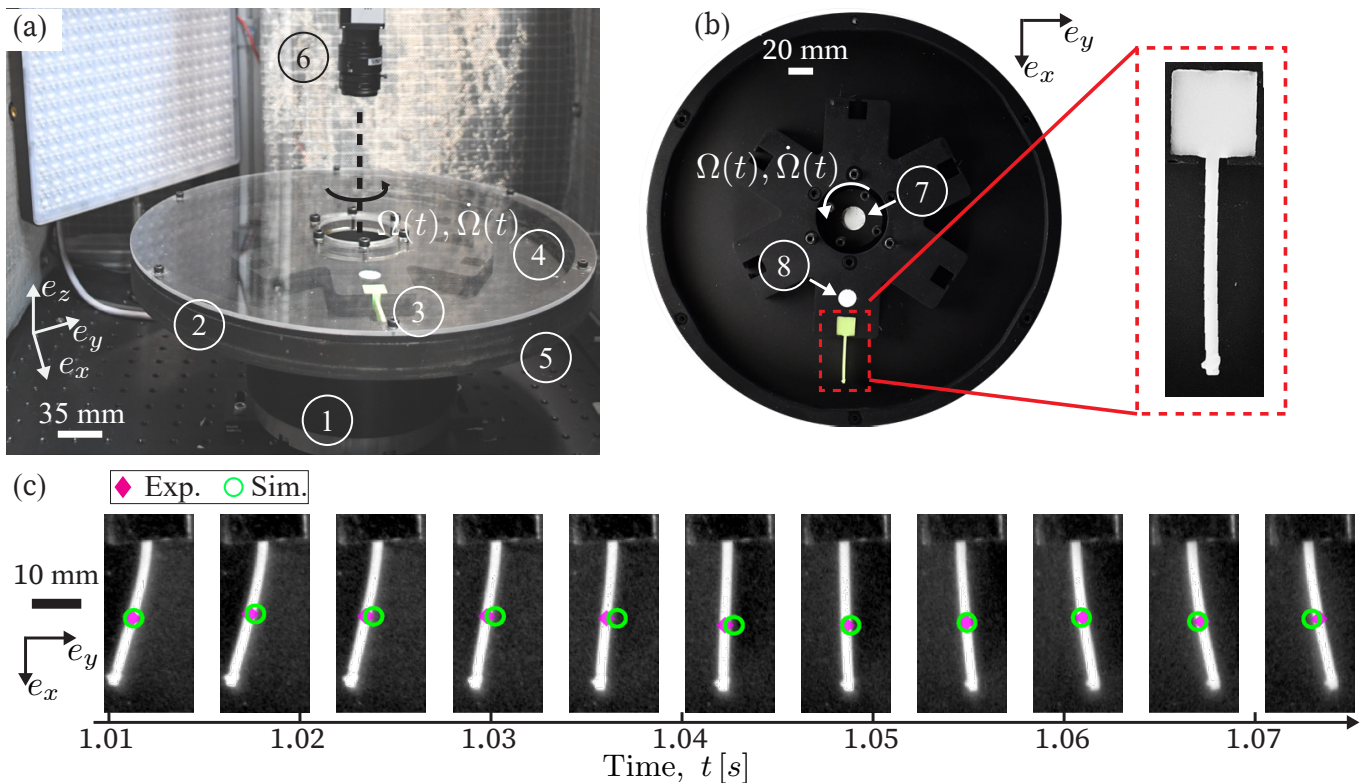


FIG. 2. Experimental apparatus. (a) Photograph of our setup: torque-controlled motor ①, rigid disk ②, cantilever beam ③, acrylic top plate ④ and bottom dish ⑤, and camera ⑥. (b) Top view showing fixed ⑦ and rotating ⑧ markers for image stabilization. Inset: Zoom-in of the sample. (c) Rotating beam frames with overlaid symbols at midspan position: experiments (magenta diamonds) and simulations (green circles) for $\Omega_0 = 15$ rad/s and $f_d = 7$ Hz.

five times to quantify uncertainties. We explore the following range of drive parameters: frequency $f_d \in [1, 8]$ Hz and mean angular velocity $\Omega_0 \in [0, 60]$ rad/s (i.e., $\mathcal{C} \in [0.03, 101]$ and $\mathcal{E} \in [0.2, 1.4]$). These ranges are set by back-electromotive force limits during deceleration.

VI. EXPERIMENTAL VALIDATION OF THE NUMERICAL MODEL

We validate the numerical model against experiments for the reference beam (Table I) by comparing time series and frequency response of the vertical midspan displacement, y_m , under different driving conditions.

Figure 3(a) shows the root-mean-square value of the nondimensional midspan displacement,

$$\text{RMS}(y_m) = \left(\frac{1}{N} \sum_{k=1}^N (y_{m,k})^2 \right)^{1/2}, \quad (16)$$

where k is the index of the sampled point, versus drive frequency $f_d \in [1, 20]$ Hz at mean angular velocity $\Omega_0 = 5$ rad/s. Experiments are limited to $f_d \leq 8$ Hz due to motor constraints (see Section V). The experimental and simulated $\text{RMS}(y_m)$ values show good agreement, both

exhibiting a clear resonant peak at $f_d \approx 7$ Hz, consistent with the first natural frequency of $f_n = 6.37$ Hz (see Section V).

Figure 3(b) shows the time series of the dimensionless midspan displacement, $y_m(\tau)$, at the resonance drive frequency $f_0 = 7$ Hz. Experiments and simulations match closely in both amplitude and frequency. The experimental curve represents the mean of five repetitions, with standard deviations smaller than the line width, indicating high reproducibility.

We also compute the power spectrum $|\text{FFT}(y_m)|$ of the midspan displacement time series. Figure 3(c) shows a representative power spectrum versus response frequency f_r for the resonant case. Both experimental and numerical spectra confirm a resonance peak at $f_r \approx 7$ Hz. The experimental spectrum exhibits higher broadband low-frequency noise, visible as an elevated baseline, due to parasitic vibrations in the apparatus.

The close agreement between experiments and simulations validates the numerical model for the parameter studies that follow.

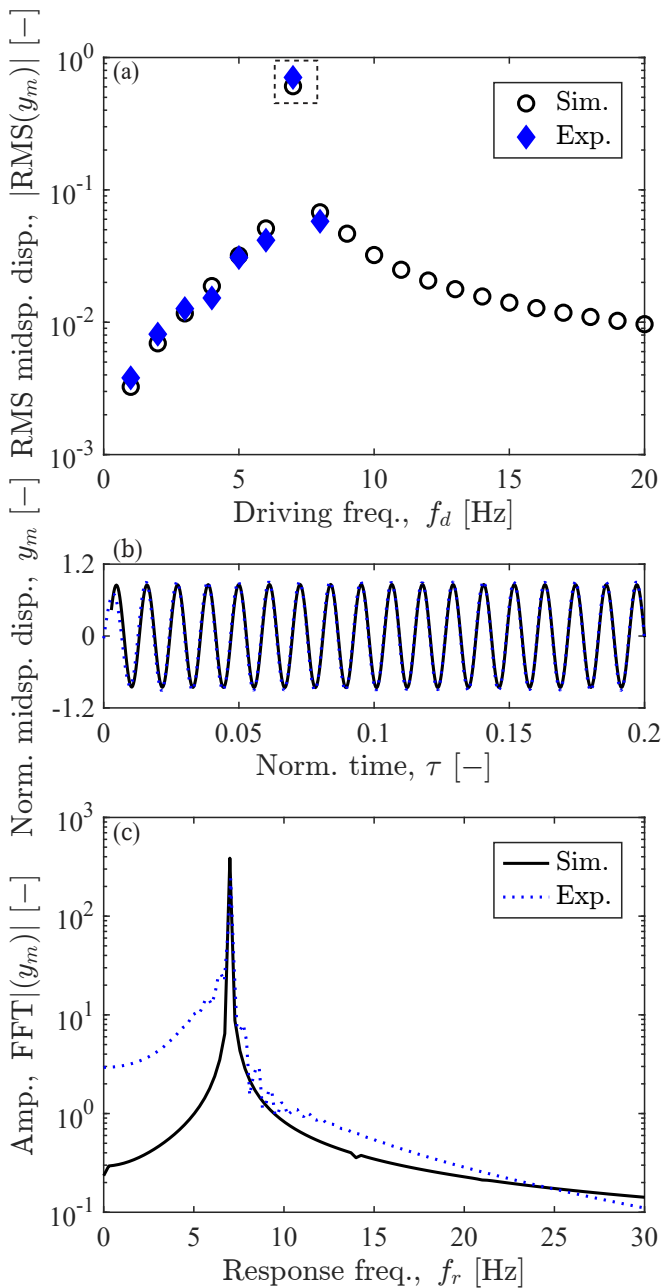


FIG. 3. Experimental validation of the numerical model (parameters in Table I). (a) Resonance curve: RMS of dimensionless midspan displacement $\text{RMS}(y_m)$ versus drive frequency f_d at mean angular velocity $\Omega_0 = 5$ rad/s. Each experimental data point is the average of five repetitions; error bars are within the symbol size. (b) Time series of dimensionless midspan displacement, $y_m(\tau)$, at $f_d = 7$ Hz. (c) Power spectrum of the time series in (b), showing resonance at 7 Hz. Symbols/lines: (a) experiments (solid diamonds), simulations (open circles); (b, c) experiments (dashed), simulations (solid).

VII. BOUNDARY BETWEEN QUASI-STATIC AND DYNAMIC RESPONSE

Having validated the numerical model, we proceed to systematically explore the parameter space. We focus on the reference beam (parameters in Table I) to characterize the boundary between quasi-static (non-inertial) and dynamic (inertial) response. To do so, we compare time series of the dimensionless midspan displacement, $y_m(\tau)$, from the full dynamical system Eqs. (8–10) and the quasi-static approximation that neglects inertial effects. (In Section VIII, we will generalize this analysis for a broader range of the system’s parameters.)

We introduce a criterion to distinguish between quasi-static and dynamic regimes based on the relative root-mean square (RMS) difference of $y_m(\tau)$. Using Eq. (16), we define

$$\text{RMS}_{\text{Dyn.}} = \text{RMS}(y_m^{\text{Dyn.}}) \quad \text{and} \quad \text{RMS}_{\text{QS}} = \text{RMS}(y_m^{\text{QS}}), \quad (17)$$

where $y_m^{\text{Dyn.}}$ and y_m^{QS} are the dimensionless midspan displacements from the dynamical and quasi-static models. The relative RMS difference is

$$\Delta\text{RMS} = \frac{|\text{RMS}_{\text{Dyn.}} - \text{RMS}_{\text{QS}}|}{\text{RMS}_{\text{Dyn.}}} \quad (18)$$

We classify the response as dynamic when $\Delta\text{RMS} \geq \Delta\text{RMS}_{\text{th}}$ and quasi-static otherwise, where $\Delta\text{RMS}_{\text{th}}$ is a threshold value. We set $\Delta\text{RMS}_{\text{th}} = 0.10$ but examine the boundary’s sensitivity to this threshold in Section VIII and Appendix D.

In Fig. 4(a,b), we plot $\text{RMS}(y_m)$ versus the normalized drive frequency, $\tilde{f}_d = f_d/f_n$, where f_n is the natural frequency defined in Eq. (7), for the reference beam. Panels (a) and (b) show results for both the dynamical (circles) and quasi-static (stars) models at angular velocities $\Omega_0 = 10$ rad/s and $\Omega_0 = 100$ rad/s, respectively. The dynamical model exhibits typical resonance (peak at $\tilde{f}_0 = f_0/f_n$, represented by the vertical dashed line), whereas the quasi-static model yields nearly linear RMS versus \tilde{f}_d . The dynamical and quasi-static RMS are nearly indistinguishable at low drive frequencies but separate before resonance (in the dynamic case). The resonance frequency \tilde{f}_0 is higher for $\Omega_0 = 100$ rad/s than for 10 rad/s. Additionally, the agreement between the quasi-static and dynamical simulations extends to higher frequencies with increasing Ω_0 , which we explore next by examining ΔRMS in Fig. 4(c,d). The open triangle, at the critical drive frequency \tilde{f}_d^* (vertical dotted line), marks the first point where $\Delta\text{RMS} \geq \Delta\text{RMS}_{\text{th}}$. For $\tilde{f}_d < \tilde{f}_d^*$ (shaded region), the response is quasi-static, whereas for $\tilde{f}_d > \tilde{f}_d^*$, the response is dynamic and the quasi-static approximation breaks down.

We now systematically explore the drive parameter space to map the transition from quasi-static to dynamic behavior. Using Eqs. (11) and (12), we quantify the harmonic driving using the *maximal* values of the centrifugal

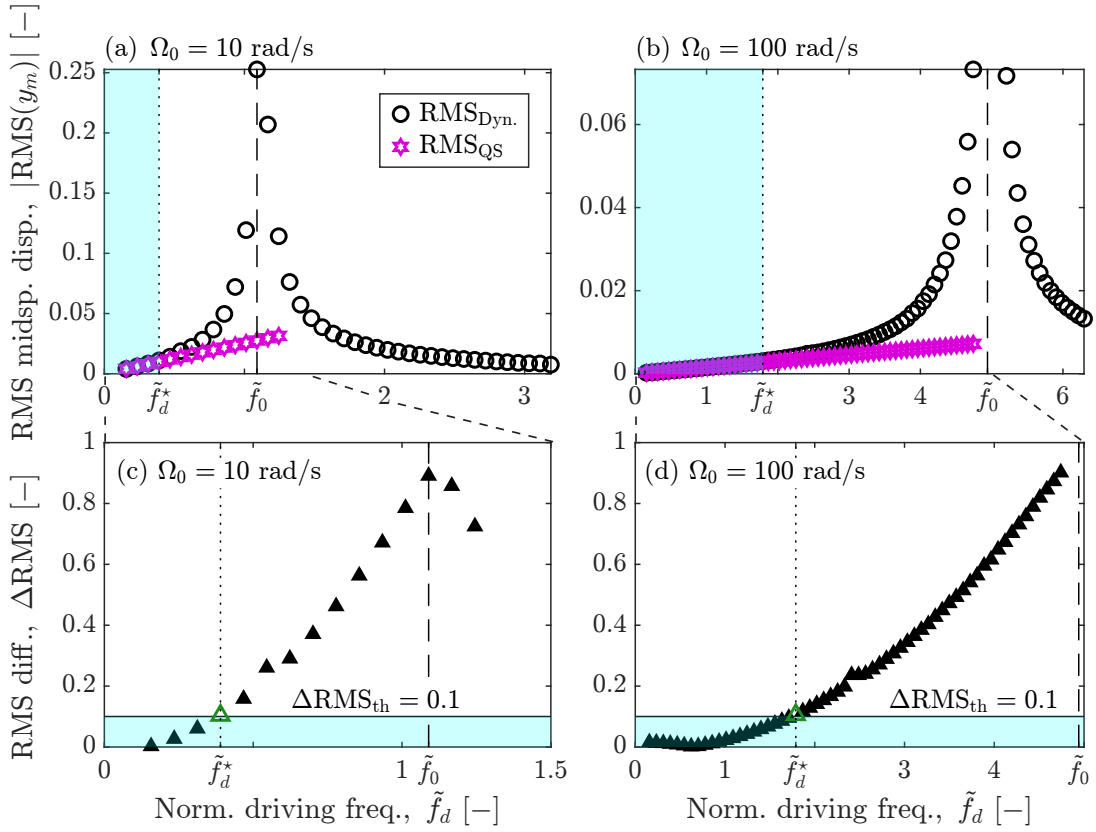


FIG. 4. Comparison of dynamical and quasi-static simulations for the reference beam. (a, b) $\text{RMS}(y_m)$ versus normalized drive frequency for $\Omega_0 = 10$ rad/s and 100 rad/s, respectively. Circles: dynamical ($\text{RMS}_{\text{Dyn.}}$); stars: quasi-static (RMS_{QS}). (c, d) Relative RMS difference, ΔRMS , for the same conditions. Vertical lines: critical normalized drive frequency \tilde{f}_d^* (dotted); normalized resonance frequency \tilde{f}_0 (dashed). Horizontal line in (c, d): threshold $\Delta\text{RMS}_{\text{th}} = 0.1$. Open triangle: first point where $\Delta\text{RMS} \geq \Delta\text{RMS}_{\text{th}}$. Shaded region: quasi-static response; unshaded: dynamic response.

and Euler numbers:

$$C_{\max} = (\Omega_0 + a)^2 \frac{\rho A R L^3}{EI} \quad \text{and} \quad (19)$$

$$\mathcal{E}_{\max} = a 2\pi f_d \frac{\rho A R L^3}{EI}. \quad (20)$$

Since the amplitude is fixed at $a = 1$ rad/s, varying the mean angular velocity, Ω_0 , modifies only C_{\max} , whereas varying the drive frequency affects only \mathcal{E}_{\max} .

With these maximal values defined, we apply the RMS-based criterion to map the quasi-static-to-dynamic boundary in the $(C_{\max}, \mathcal{E}_{\max})$ plane, as plotted in Fig. 5(a). Each triangle denotes the first pair of simulations (dynamical and quasi-static) for which $\Delta\text{RMS} \geq 0.10$. The data are obtained by fixing C_{\max} (equivalently, Ω_0) and running both dynamical and quasi-static simulations while increasing \mathcal{E}_{\max} by linearly increasing f_d . From the critical drive frequency, \tilde{f}_d^* (see Fig. 4), we obtain the critical maximal Euler number, \mathcal{E}^* , through Eq. (20). The $\mathcal{E}^*(C_{\max})$ curve partitions the parameter space into two regions: a quasi-static region (lower, shaded), where inertial effects are negligible, and a dynamic region (upper, unshaded), where inertial effects

dominate. For $C_{\max} \lesssim 10$, the critical maximal Euler number remains nearly constant at $\mathcal{E}^* \approx 5$, after which it scales as $\mathcal{E}^* \sim C_{\max}^{1/2}$.

The shape of this $\mathcal{E}^*(C_{\max})$ boundary reveals two key behaviors. For a given Euler number, increasing the centrifugal number (moving right in the phase diagram) eventually produces quasi-static response for sufficiently large C_{\max} . Conversely, for a given centrifugal number, increasing the Euler number (moving upwards in the phase diagram) eventually produces dynamic response with non-negligible inertial effects for sufficiently large \mathcal{E}_{\max} .

To illustrate the breakdown of the quasi-static approximation in the dynamic regime, Fig. 5(b, c) plots representative time series of the dimensionless midspan displacement for two parameter pairs: $(C_{\max}, \mathcal{E}_{\max}) = (50, 2)$ and $(50, 1)$, corresponding to locations just above and below the \mathcal{E}^* boundary, respectively. As expected from their location relative to the boundary, the dynamical and quasi-static simulations disagree in panel (b) (dynamic regime), whereas they agree well in panel (c) (quasi-static regime).

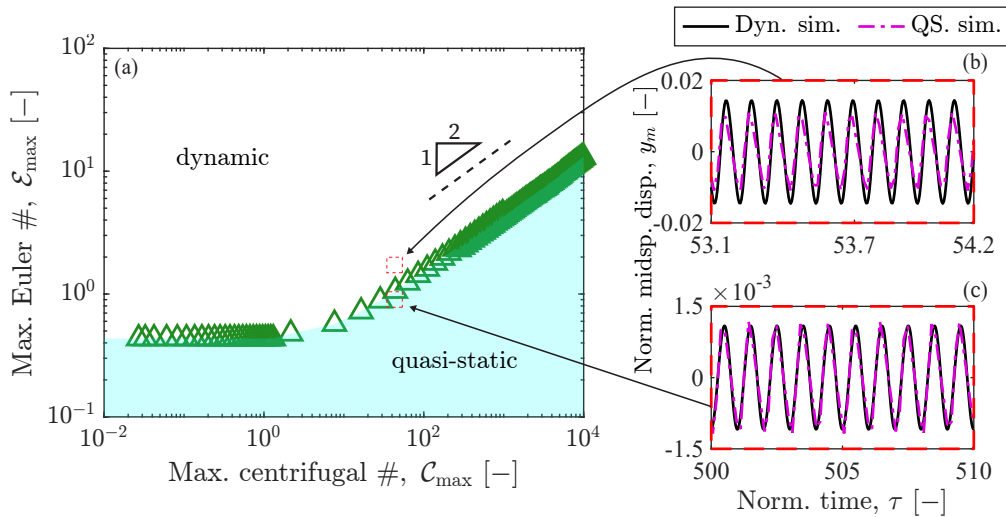


FIG. 5. Phase diagram of quasi-static and dynamic regions for the reference beam. (a) Critical maximal Euler number \mathcal{E}^* (triangles) versus maximal centrifugal number C_{\max} separates quasi-static (shaded) and dynamic (unshaded) regions. (b, c) Time series of dimensionless midspan displacement: dynamical (solid) and quasi-static (dashed) for $C_{\max} \approx 50$ with (b) $\mathcal{E}_{\max} \approx 2$ (above \mathcal{E}^*) and (c) $\mathcal{E}_{\max} \approx 1$ (below \mathcal{E}^*).

The square-root scaling $\mathcal{E}^* \sim C_{\max}^{1/2}$ observed in the phase boundary is related to how centrifugal loading affects the beam's resonance frequency. In Fig. 6, we plot

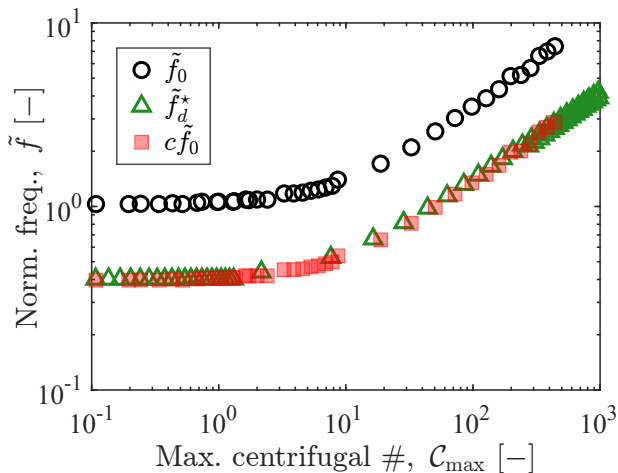


FIG. 6. Normalized resonance frequency \tilde{f}_0 (circles), critical normalized drive frequency \tilde{f}_d^* (triangles), and the relation $\tilde{f}_d^* = c\tilde{f}_0$ with constant $c < 1$ (squares) versus centrifugal number C_{\max} from dynamical simulations of the reference beam. The constant is determined to be $c = 0.385 \pm 0.001$ through a nonlinear least-squares fit, as described in Section VIII.

the normalized resonance frequency \tilde{f}_0 , the critical frequency \tilde{f}_d^* , and the linear relation $\tilde{f}_d^* = c\tilde{f}_0$ as functions of C_{\max} . The proportionality constant is determined to be $c = 0.385 \pm 0.001$ by nonlinear least-squares fitting using

the MATLAB function `lsqcurvefit` (see Section VIII). The results in Fig. 6 suggest that the critical frequency corresponds to the resonance frequency scaled by the factor c .

For $C_{\max} \lesssim 8$, the resonance frequency remains constant at $\tilde{f}_0 \approx 1$, whereas for $C_{\max} \gtrsim 8$, it scales as $\tilde{f}_0 \sim C_{\max}^{1/2}$. The critical frequency \tilde{f}_d^* exhibits qualitatively similar behavior. This increase in frequency with angular velocity is attributed to the classical centrifugal stiffening effect: rotation induces axial tension in the beam, thereby increasing its natural frequency. [36] derived exact solutions for centrifugally stiffened beams; [37] reported natural frequency changes versus angular velocity and geometry; [5] demonstrated how rotation-induced axial force affects shaft frequency. These studies validate the classical Southwell relation [31] and its associated square-root scaling, which our rotating system also exhibits. This scaling proves central to the phase boundary in Fig. 5 and motivates the theoretical analysis in the next section.

VIII. GENERALIZED THEORETICAL DESCRIPTION OF THE PHASE BOUNDARY

Having established the transition between quasi-static and dynamic behavior for our reference beam (Table I), we now develop a theoretical description for the phase boundary between these regimes. The starting point for our analysis is the premise that the physical mechanism driving this boundary is the well-known centrifugal stiffening effect [31]. For ease of notation, we define

$G = \rho A R L^3 / EI$, combining geometric and mechanical parameters, such that

$$\mathcal{E}_{\max} = Ga2\pi f_d, \quad \text{and} \quad (21)$$

$$\mathcal{C}_{\max} = G(\Omega_0 + a)^2. \quad (22)$$

We recall that the critical maximal Euler number is

$$\mathcal{E}^* = Ga2\pi f_d^*. \quad (23)$$

Furthermore, aligning with the data in Fig. 4, we posit that the critical driving frequency follows

$$f_d^* = cf_0, \quad (24)$$

where f_0 is the resonance frequency and $c < 1$ is a proportionality constant. While the critical ratio $c = f_d^*/f_0$ is commonly used in the literature as a heuristic criterion for the quasi-static/dynamic boundary [7, 24], in Appendix E, using a canonical second-order dynamical system, we show that c is set by the chosen error threshold and remains constant for sufficiently underdamped systems. Given the underdamped nature of our system, the theoretical argument presented in Appendix E rationalizes the constant proportionality posited in Eq. (24) and observed in the data plotted in Fig. 4.

The classical Southwell equation determines that rotation shifts the resonance frequency due to centrifugal stiffening. Following [31], the maximal shifted resonance frequency of the first vibrational mode for a beam rotating with angular velocity Ω is

$$(2\pi f_0)^2 = (2\pi f_n)^2 + S_1 \Omega^2. \quad (25)$$

The first Southwell coefficient S_1 (a geometric parameter dependent on the beam's fundamental mode shape) [4] is computed using an established analytical expression derived from the Rayleigh quotient, defined as the ratio of the potential energy due to centrifugal tension to the kinetic energy of the first mode [21, 22, 31]. Substituting the maximal angular velocity in our system ($\Omega_0 + a$) into Eq. (25) we find the maximal resonance frequency

$$(2\pi f_0)^2 = (2\pi f_n)^2 + S_1(\Omega_0 + a)^2. \quad (26)$$

Substituting Eqs. (24) and (26) into Eq. (23) yields

$$\begin{aligned} (\mathcal{E}^*)^2 &= (Ga2\pi cf_0)^2 \\ &= (Gac)^2 [(2\pi f_n)^2 + S_1(\Omega_0 + a)^2], \end{aligned} \quad (27)$$

which we then rewrite in terms of the centrifugal and Euler numbers:

$$(\mathcal{E}^*)^2 = c^2 (\mathcal{E}_n^2 + S_1 Ga^2 \mathcal{C}_{\max}), \quad (28)$$

where \mathcal{E}_n denotes the maximal Euler number at $f_d = f_n$. Since we are interested only in the positive solutions, we write

$$\mathcal{E}^* = c\sqrt{\mathcal{E}_n^2 + S_1 Ga^2 \mathcal{C}_{\max}}. \quad (29)$$

We validate Eq. (29) by conducting numerical simulations over a broad range of material and geometric parameters in the following ranges: Young's modulus $E \in [10^5, 10^9]$ Pa, beam length $L \in [10^{-4}, 10^{-2}]$ m, and thickness-to-length slenderness ratio $\lambda_1 = h/L \in [10^{-1}, 10^{-2}]$.

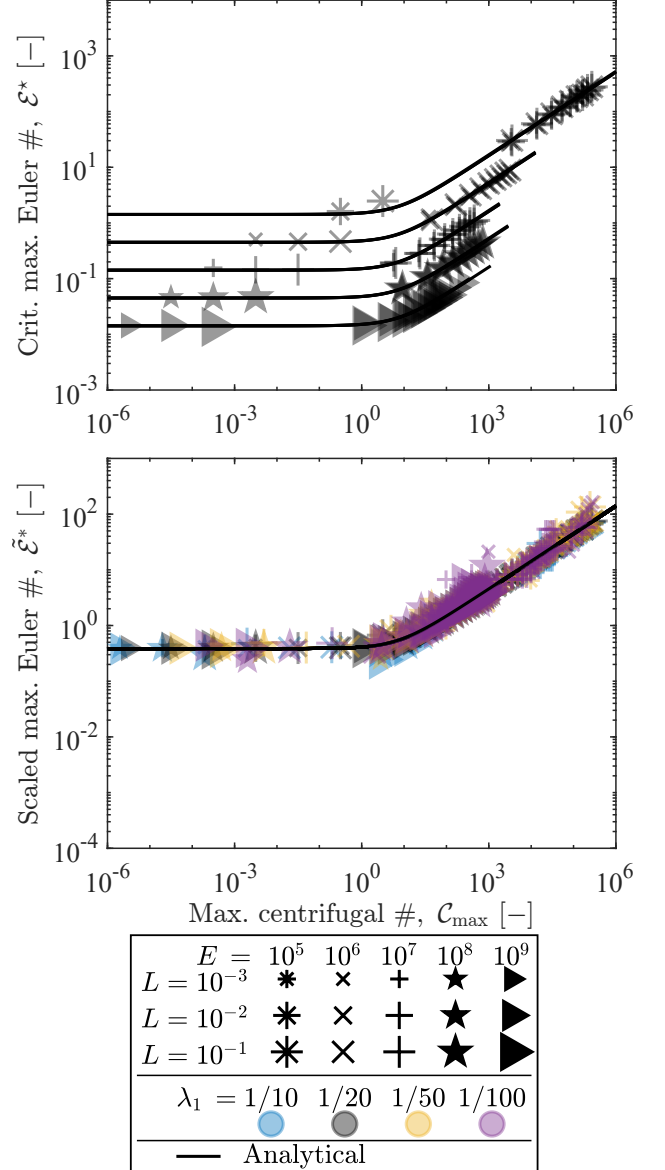


FIG. 7. The quasi-static/dynamic boundary for varying Young's moduli, lengths, and slenderness ratios. (a) The critical maximal Euler number \mathcal{E}^* , and (b) the scaled maximal Euler number $\tilde{\mathcal{E}}^*$ as functions of the maximal centrifugal number \mathcal{C}_{\max} . Symbols denote different values of Young's modulus; larger marker sizes indicate longer beams; and colors indicate slenderness ratio, with $\lambda_1 = 1/20$ in (a). The analytical solutions from Eq. (29) and Eq. (30) are shown as black solid lines in (a) and (b), respectively.

In Fig. 7(a), we plot the critical maximal Euler number versus maximal centrifugal number $\mathcal{E}^*(\mathcal{C}_{\max})$ for dif-

ferent values of E and L , and with $\lambda_1 = 1/20$, maintaining the threshold $\Delta\text{RMS}_{\text{th}} = 0.10$. The predictions from Eq. (29) (black solid line) are in excellent agreement with the numerical data. Different values of E introduce a multiplicative pre-factor that shifts the data vertically in the log-log plot. Since this shift stems from the beams' differing natural frequencies, we rescale the numerical results and Eq. (29) by $1/\mathcal{E}_n$, yielding the scaled maximal Euler number:

$$\tilde{\mathcal{E}}^* = \frac{\mathcal{E}^*}{\mathcal{E}_n} = c \sqrt{1 + \frac{S_1 G a^2}{\mathcal{E}_n^2} C_{\text{max}}}, \quad (30)$$

where, we recall that $c = 0.385 \pm 0.001$. In Fig. 7(b), we plot the scaled quantity for the full range of E , L , and λ_1 explored. The analytical expression in Eq. (30) (black solid line) collapses all data onto a master curve, confirming that the phase boundary is fully described by the natural frequency shift due to centrifugal stiffening.

IX. CONCLUSIONS AND FUTURE WORK

We adapted an *elastica*-based reduced-order model and validated it against precision experiments to simulate rotating cantilever beams driven harmonically. Systematically exploring the parameter space, we identified two distinct regimes: one quasi-static, where inertial effects remain negligible under unsteady harmonic driving, and another dynamic, where inertia significantly influences the response. We characterized the boundary between these regimes using the Euler and centrifugal numbers, which quantify centrifugal and Euler forces relative to characteristic bending forces. The critical Euler number remains approximately constant at low centrifugal numbers but transitions to square-root scaling with centrifugal number at higher rotation rates.

We derived a predictive theoretical description for this transition, revealing that centrifugal stiffening governs the scaling. Counterintuitively, faster rotation produces less dynamic response: increasing rotation raises the beam's resonance frequency, making the beam effectively stiffer and expanding the quasi-static regime to higher drive frequencies.

Our results establish the conditions under which a quasi-static approximation remains valid for rotating flexible beams under unsteady loading. This framework can be applied to the design and control of robotic arms, turbine blades, soft actuators, and deployable aerospace components.

Future work should investigate more complex nonlinear phenomena such as modal interactions and potential instabilities. Preliminary observations suggest the system exhibits complex dynamics, potentially including chaos, under certain driving conditions, warranting further investigation.

Appendix A: Discretized equations of motion

We define $N + 1$ uniform grid points along the dimensionless arclength $s_i = i\Delta s$ with $\Delta s = 1/N$. At each grid point, we define discretized coordinates $\theta_i = \theta(s_i)$, $x_i = x(s_i)$, $y_i = y(s_i)$, and solve for θ_i to avoid enforcing the inextensibility constraint at each step. Using the discrete version of the kinematic relations in Eq. (1), the discrete Cartesian coordinates (x_i, y_i) are computed with the trapezoid rule. For every x_i with $i = 1, \dots, N-1$ we get

$$x_i = \frac{\Delta s}{2} \sum_{k=1}^i \cos \theta_{k-1} + \cos \theta_k \quad (A1)$$

and conducting this integration for every i yields the linear system

$$\begin{aligned} \mathbf{x} &= [x_1 \ x_2 \ \cdots \ x_{N-1}]^T \\ &= \left(\frac{\Delta s}{2} \mathbf{L} \cdot \tilde{\mathbf{c}} \right), \end{aligned} \quad (A2)$$

where \mathbf{L} is the lower triangular matrix

$$\mathbf{L} = \frac{\Delta s}{2} \begin{pmatrix} 1 & 0 & 0 & \cdots & 0 \\ 2 & 1 & 0 & \cdots & 0 \\ 2 & 2 & 1 & \cdots & 0 \\ \vdots & \vdots & \vdots & \ddots & \vdots \\ 2 & 2 & 2 & \cdots & 1 \end{pmatrix}, \quad (A3)$$

and

$$\tilde{\mathbf{c}} = [\cos \theta_1 \ \cdots \ \cos \theta_{N-1}]^T. \quad (A4)$$

Similarly, for the y -coordinate, we find

$$\mathbf{y} = [y_1 \ y_2 \ \cdots \ y_{N-1}]^T = (\mathbf{L} \cdot \tilde{\mathbf{s}}), \quad (A5)$$

where

$$\tilde{\mathbf{s}} = [\sin \theta_1 \ \cdots \ \sin \theta_{N-1}]^T. \quad (A6)$$

The first and second time derivatives of \mathbf{x} and \mathbf{y} are

$$\begin{aligned} \dot{\mathbf{x}} &= -\mathbf{L} \left(\tilde{\mathbf{S}}_1 \cdot \dot{\Theta} \right), \\ \ddot{\mathbf{x}} &= -\mathbf{L} \left(\tilde{\mathbf{S}}_1 \cdot \ddot{\Theta} + \tilde{\mathbf{C}}_1 \cdot \dot{\Theta}^2 \right), \\ \dot{\mathbf{y}} &= \mathbf{L} \left(\tilde{\mathbf{C}}_1 \cdot \dot{\Theta} \right), \\ \ddot{\mathbf{y}} &= \mathbf{L} \left(\tilde{\mathbf{C}}_1 \cdot \ddot{\Theta} - \tilde{\mathbf{S}}_1 \cdot \dot{\Theta}^2 \right), \end{aligned} \quad (A7)$$

where $\dot{\Theta}$ and $\ddot{\Theta}$ are the first and second time derivatives of $\Theta = [\theta_1, \dots, \theta_{N-1}]$, and $\dot{\Theta}^2 = [\dot{\theta}_1^2, \dots, \dot{\theta}_{N-1}^2]$. In

Eq. (A7), $\tilde{\mathbf{S}}_1$ and $\tilde{\mathbf{C}}_1$ are the diagonal matrices:

$$\tilde{\mathbf{S}}_1 = \begin{pmatrix} \sin \theta_1 & 0 & \cdots & 0 \\ 0 & \sin \theta_2 & \cdots & 0 \\ \vdots & \vdots & \ddots & 0 \\ 0 & 0 & \cdots & \sin \theta_{N-1} \end{pmatrix}, \quad (\text{A8})$$

$$\tilde{\mathbf{C}}_1 = \begin{pmatrix} \cos \theta_1 & 0 & \cdots & 0 \\ 0 & \cos \theta_2 & \cdots & 0 \\ \vdots & \vdots & \ddots & 0 \\ 0 & 0 & \cdots & \cos \theta_{N-1} \end{pmatrix}. \quad (\text{A9})$$

Enforcing Neumann boundary condition $\theta(1, \tau)_{,s} = 0$ with the backwards Euler method we obtain

$$\frac{\theta_N - \theta_{N-1}}{\Delta s} = 0. \quad (\text{A10})$$

Applying Eq. (A10) together with the boundary condition $\theta_0 = 0$ at the clamped end, we simplify the system to solve for $N-1$ grid points.

We now discretize the tension equations in Eqs. (8-9) with zero tension at the free end, $s = 1$.

$$n_x = - \int_s^1 \left(\ddot{x} + \eta \dot{x} - 2\mathcal{I} \dot{y} - [\mathcal{C}(1 - \delta + \delta x) + \delta \mathcal{E} y] \right) ds \quad (\text{A11})$$

$$n_y = - \int_s^1 \left(\ddot{y} + \eta \dot{y} + 2\mathcal{I} \dot{x} + [\mathcal{E}(1 - \delta + \delta x) - \delta \mathcal{C} y] \right) ds$$

Substituting Eqs. (A2), (A5) and (A7) into Eq. (A11) and rearranging yields

$$n_x = \mathcal{C} \left[1 + (\delta - 1) \mathbf{s} - \delta \frac{\mathbf{s}^2}{4} \right] + \mathbf{UL} \left[\tilde{\mathbf{S}}_1 \ddot{\Theta} + \tilde{\mathbf{C}}_1 \dot{\Theta}^2 + \left(\eta \tilde{\mathbf{S}}_1 + 2\mathcal{I} \tilde{\mathbf{C}}_1 \right) \dot{\Theta} + \delta (\mathcal{C} \tilde{\mathbf{c}} + \mathcal{E} \tilde{\mathbf{s}}) \right] \quad (\text{A12})$$

$$n_y = -\mathcal{E} \left[1 + (\delta - 1) \mathbf{s} - \delta \frac{\mathbf{s}^2}{4} \right] - \mathbf{UL} \left[\tilde{\mathbf{C}}_1 \ddot{\Theta} - \tilde{\mathbf{S}}_1 \dot{\Theta}^2 + \left(\eta \tilde{\mathbf{C}}_1 - 2\mathcal{I} \tilde{\mathbf{S}}_1 \right) \dot{\Theta} + \delta (\mathcal{E} \tilde{\mathbf{c}} - \mathcal{C} \tilde{\mathbf{s}}) \right], \quad (\text{A13})$$

where \mathbf{U} is the upper triangular matrix

$$\mathbf{U} = \frac{\Delta s}{2} \begin{pmatrix} 1 & 2 & 2 & \cdots & 3 \\ 0 & 1 & 2 & \cdots & 3 \\ 0 & 0 & 1 & \cdots & 3 \\ \vdots & \vdots & \vdots & \ddots & \vdots \\ 0 & 0 & 0 & \cdots & 2 \end{pmatrix} \quad (\text{A14})$$

and $\mathbf{s} = [s_1, \dots, s_{N-1}]$ is the discretized arclength. Next, we discretize the moment Eq. (10). Using center differences, applying the boundary conditions and Eq. (A10) we find

$$\theta_{,s} = -\mathbf{K} \Theta, \quad (\text{A15})$$

where \mathbf{K} is the stiffness matrix

$$\mathbf{K} = -\frac{1}{\Delta s} \begin{pmatrix} -2 & 1 & 0 & 0 & \cdots & 0 \\ 1 & -2 & 1 & 0 & \cdots & 0 \\ 0 & 1 & -2 & 1 & \cdots & 0 \\ \vdots & \vdots & \vdots & \vdots & \ddots & \vdots \\ \vdots & \vdots & \vdots & 1 & -2 & 1 \\ 0 & 0 & 0 & 0 & 1 & -1 \end{pmatrix}. \quad (\text{A16})$$

Substituting Eqs. (A12-A15) into Eqs. (8-10), applying trigonometric identities, and rearranging, we obtain the discretized equations of motion in Eq. (15) in terms of the tangent angle θ_i , which we rewrite as:

$$\mathbf{M} \ddot{\Theta} + \mathbf{C} \dot{\Theta} + \mathbf{K} \Theta = \mathbf{f}. \quad (\text{A17})$$

The mass matrix \mathbf{M} decomposes as $\mathbf{M} = \mathbf{UL}\tilde{\mathbf{C}}$, where \mathbf{U} and \mathbf{L} are the upper and lower triangular matrices in Eqs. (A3) and (A14). The matrix $\tilde{\mathbf{C}}$ encodes cosines of tangent-angle differences $\Delta\theta_{i,j} = \theta_j - \theta_i$ between nodes i and j . To simplify notation we define $c_{i,j} = \cos \Delta\theta_{i,j}$, and $s_{i,j} = \sin \Delta\theta_{i,j}$:

$$\tilde{\mathbf{C}} = \begin{pmatrix} 1 & c_{1,2} & c_{1,3} & \cdots & c_{1,N-1} \\ c_{1,2} & 1 & c_{2,3} & \cdots & c_{2,N-1} \\ c_{1,3} & c_{2,3} & 1 & \cdots & c_{3,N-1} \\ \vdots & \vdots & \vdots & \ddots & \vdots \\ c_{1,N-1} & c_{2,N-1} & c_{3,N-1} & \cdots & 1 \end{pmatrix}. \quad (\text{A18})$$

The damping matrix is $\mathbf{C} = \eta \mathbf{M} + 2\mathcal{I} \mathbf{B}$. Here, $\mathbf{B} = \mathbf{UL}\tilde{\mathbf{S}}$ is the gyroscopic matrix, which represents the Coriolis forces acting on the beam through the nondimensional inertial number \mathcal{I} . This matrix arises from the spatial integration of geometric coupling terms defined by

$$\tilde{\mathbf{S}} = \begin{pmatrix} 0 & s_{1,2} & s_{1,3} & \cdots & s_{1,N-1} \\ s_{1,2} & 0 & s_{2,3} & \cdots & s_{2,N-1} \\ s_{1,3} & s_{2,3} & 0 & \cdots & s_{3,N-1} \\ \vdots & \vdots & \vdots & \ddots & \vdots \\ s_{1,N-1} & s_{2,N-1} & s_{3,N-1} & \cdots & 0 \end{pmatrix}. \quad (\text{A19})$$

However, while the Coriolis term is formally included in the derivation, its effects are ultimately shown to be negligible. The forcing term \mathbf{f} contains the gyroscopic nonlinearities $\dot{\Theta}^2$ and trigonometric nonlinearities from the diagonal matrices $\tilde{\mathbf{S}}_1, \tilde{\mathbf{C}}_1$ in Eqs. (A8) and (A9), and decomposes as

$$\mathbf{f} = -\mathbf{B} \dot{\Theta}^2 - \mathbf{UL} \delta \mathcal{E} \mathbf{e} + \left[1 + (\delta - 1) \mathbf{s} - \delta \frac{\mathbf{s}^2}{4} \right] (\mathcal{E} \tilde{\mathbf{C}}_1 - \mathcal{C} \tilde{\mathbf{S}}_1). \quad (\text{A20})$$

This term appears in the right hand side of Eq. (15).

Appendix B: Damping coefficient

The damping coefficient of an underdamped unforced system is $\gamma = |2\rho A/t_{\text{decay}}|$ [32]. We determine the damping coefficient by perturbing the beam from equilibrium and measuring a time series of the horizontal deflection at midspan. The decay time t_{decay} is extracted by fitting the exponential function $A \exp(-t/t_{\text{decay}})$ to the signal. We find that $\gamma = 0.039 \pm 0.008$. For the dimensionless Eqs. (8–10), we nondimensionalize the damping coefficient as $\eta = \gamma L^2/\sqrt{\rho A E I}$.

Appendix C: Convergence test for grid points N

We determine the appropriate number of grid points, N , through convergence tests using drive frequencies $f_d \in [1, 10]$ Hz and mean angular velocities $\Omega_0 \in [10, 100]$ rad/s. We compute the RMS of the dimensionless midspan displacement $\text{RMS}(y_m)$ (see Eq. (16)) for $N \in [5, 80]$ grid points. Figure 8 shows that for $N \gtrsim 40$, the RMS amplitude converges.

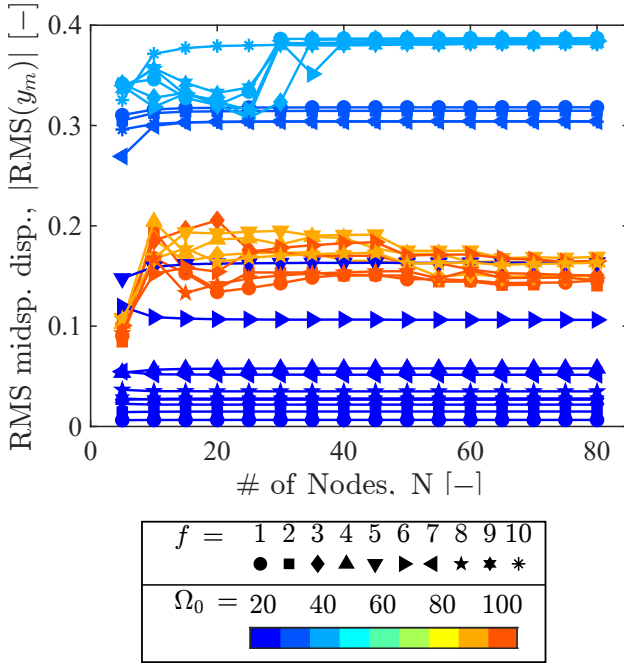


FIG. 8. Convergence test for the number of grid points N using drive frequencies $f_d \in [1, 10]$ Hz and mean angular velocities $\Omega_0 \in [10, 100]$ rad/s.

Appendix D: Effects of threshold $\Delta\text{RMS}_{\text{th}}$

We investigate the effect of the threshold $\Delta\text{RMS}_{\text{th}}$ by repeating the numerical simulations from Section VIII with $\Delta\text{RMS}_{\text{th}} = 0.05, 0.07, 0.10, 0.12$, and $\lambda_1 = 1/20$. The resulting boundaries are shown in Fig. 9. As

$\Delta\text{RMS}_{\text{th}}$ increases, the curves shift slightly upward in the log-log plot, indicating that the multiplicative constant c that determines the plateau value $\tilde{\mathcal{E}}_0^* = (\pi\lambda_1 A L^3 \sqrt{\rho}/\beta_1^2 I \sqrt{3E}) c f_n$ in the limit $C_{\text{max}} \rightarrow 0$ depends on the chosen $\Delta\text{RMS}_{\text{th}}$. The extracted constants are $c = 0.311 \pm 0.001, 0.345 \pm 0.001, 0.385 \pm 0.001, 0.404 \pm 0.001$ for $\Delta\text{RMS}_{\text{th}} = 0.05, 0.07, 0.10, 0.12$, respectively. Throughout the main text, we use the threshold value $\Delta\text{RMS}_{\text{th}} = 0.10$ (black upward triangles).

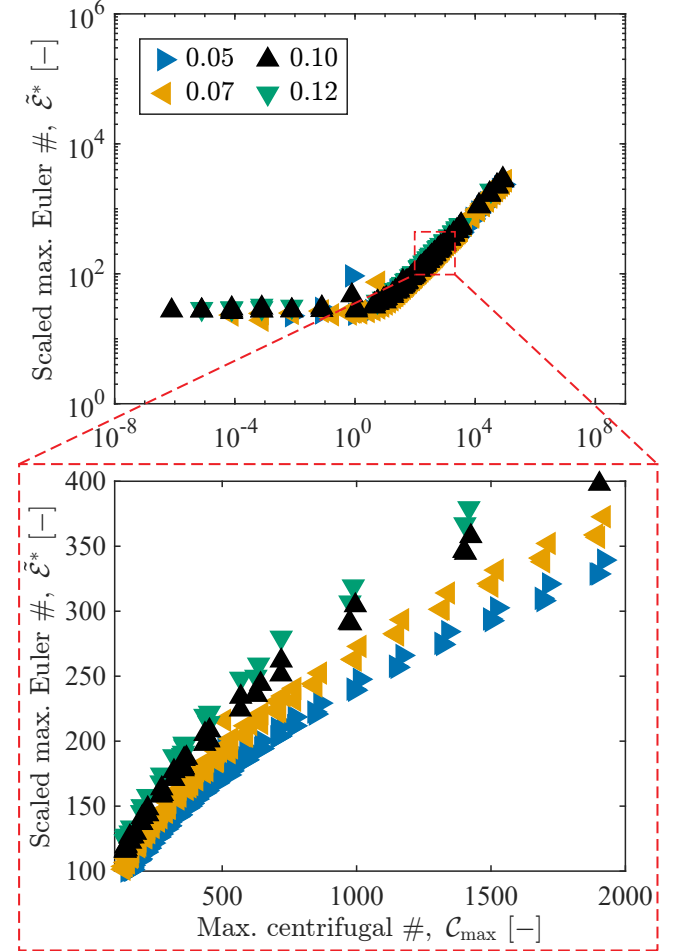


FIG. 9. Quasi-static/dynamic boundary for varying Young's moduli, lengths, and $\Delta\text{RMS}_{\text{th}}$. (a) Scaled maximal Euler number $\tilde{\mathcal{E}}^*$ versus the maximal centrifugal number C_{max} . (b) Magnified version of panel (a), focusing on the range $\tilde{\mathcal{E}}^* \in [100, 400]$, $C_{\text{max}} \in [100, 2000]$. Blue right-pointing, orange left-pointing, black upward, and green downward triangles correspond to $\Delta\text{RMS}_{\text{th}} = 0.05, 0.07, 0.10, 0.12$, respectively.

Appendix E: Quasi-static condition of the canonical second-order dynamical system

We apply classic dynamical systems theory to relate the threshold criterion ($\Delta\text{RMS}_{\text{th}}$) to the frequency ra-

tio $c_0 = f/f_n$ defined in Eq. (24). Consider the viscously damped, harmonically forced canonical second-order nondimensional dynamical system [16]:

$$\frac{d^2u}{d\tau^2} + 2\zeta \frac{du}{d\tau} + u = \frac{F_0}{k} \cos(c_0\tau) \quad (\text{E1})$$

where ζ is the nondimensional viscous damping ratio, F_0 is the drive amplitude, and k represents the system stiffness. Eq. (E1) governs the motion of various driven physical systems [27]. Table II summarizes the physical interpretation of these generalized constants for a driven mass-spring system, a pendulum, and a cantilevered elastic beam. In this table, k_s denotes the linear spring constant, m the mass, g the gravitational acceleration, and L the characteristic length. Following the definitions in the main text, E , I , ρ , A , γ , and β_1 represent Young's modulus, area moment of inertia, density, cross-sectional area, the viscous damping coefficient, and the modal constant, respectively.

	ζ	k	f_n
Mass-spring	$\gamma/(2\sqrt{k_s m})$	k_s	$\sqrt{k_s/m}$
Pendulum	$\gamma/(2mL\sqrt{gL})$	mgL	$\sqrt{g/L}$
Cantilever beam	$\gamma L^2/(2\beta_1^2\sqrt{EI\rho A})$	$3EI/L^3$	$\beta_1^2\sqrt{EI/(\rho AL^4)}$

TABLE II. Physical interpretation of nondimensional parameters for a driven mass-spring, pendulum, and cantilever beam. All are described by Eq. (E1).

The steady-state amplitudes of the dynamic and quasi-static responses, A_{dyn} and A_{QS} respectively, are derived from the magnitude of the complex exponential solution to Eq. (E1), and are given by [11]:

$$A_{\text{dyn}} = \frac{F_0/k}{\sqrt{(1-c_0^2)^2 + (2\zeta c_0)^2}} \quad \text{and} \quad (\text{E2})$$

$$A_{\text{QS}} = \frac{F_0}{k}. \quad (\text{E3})$$

Applying the criterion defined in Section VII – cf. Eq. (18), we find:

$$\begin{aligned} \Delta\text{RMS} &= \frac{A_{\text{dyn}} - A_{\text{QS}}}{A_{\text{dyn}}} \\ &= 1 - \sqrt{(1-c_0^2)^2 + (2\zeta c_0)^2}. \end{aligned} \quad (\text{E4})$$

Setting $\Delta\text{RMS}_{\text{th}} = 0.1$, we obtain the following bi-quadratic equation in terms of c_0 :

$$c_0^4 + (4\zeta^2 - 2)c_0^2 + 0.19 = 0. \quad (\text{E5})$$

In Fig. 10, we plot the solution to Eq. (E5) for the frequency ratio c_0 versus the normalized damping ζ . For sufficiently underdamped systems ($\zeta \ll 1$), the critical frequency ratio remains approximately constant at $c_0 \approx 0.31$. The reference beam in Table I has $\zeta \approx 0.017$, well within this $\zeta \ll 1$ regime. Table III tabulates c_0

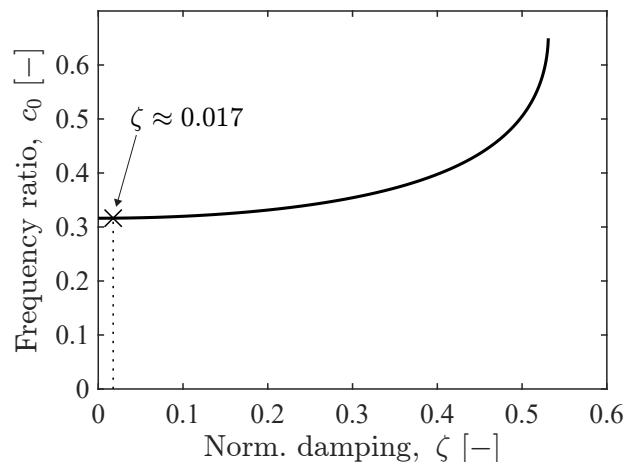


FIG. 10. The critical frequency ratio $c_0 = f/f_n$ for $\Delta\text{RMS}_{\text{th}} = 0.1$ as a function of nondimensional damping ζ for the canonical viscously damped, harmonically forced second-order system.

values in the limit $\zeta \rightarrow 0$ for various thresholds $\Delta\text{RMS}_{\text{th}}$, demonstrating that the critical frequency ratio is constant for a fixed threshold in underdamped systems. These results rationalize the linear relation $f_d^* = c f_0$ observed in the main text (cf. Fig. 6).

$\Delta\text{RMS}_{\text{th}}$	c_0
0.02	0.1414
0.04	0.2000
0.06	0.2449
0.08	0.2828
0.10	0.3162

TABLE III. Critical frequency ratio c_0 for a sufficiently underdamped system for the threshold values $\Delta\text{RMS}_{\text{th}} = 0.02, 0.04, 0.06, 0.08, 0.1$.

-
- [1] Ahmed, M.R., El Damatty, A.A., Dai, K., Ibrahim, A., Lu, W., 2022. Parametric study of the quasi-static response of wind turbines in downburst conditions using a numerical model. *Engineering Structures* 250, 113440.
- [2] Apiwattanalungarn, P., Shaw, S.W., Pierre, C., Jiang, D., 2003. Finite-element-based nonlinear modal reduction of a rotating beam with large-amplitude motion. *Journal of Vibration and Control* 9, 235–263.
- [3] Baek, C., Johanns, P., Sano, T.G., Grandgeorge, P., Reis, P.M., 2021. Finite element modeling of tight elastic knots. *Journal of Applied Mechanics* 88, 024501.
- [4] Bazoune, A., 2005. Relationship between softening and stiffening effects in terms of southwell coefficients. *Journal of sound and vibration* 287, 1027–1030.
- [5] Behzad, M., Bastami, A., 2004. Effect of centrifugal force on natural frequency of lateral vibration of rotating shafts. *Journal of sound and vibration* 274, 985–995.
- [6] Burton, T., Jenkins, N., Sharpe, D., Bossanyi, E., 2011. *Wind energy handbook*. John Wiley & Sons.
- [7] Chopra, A., 2012. *Dynamics of structures: theory and applications to earthquake engineering*. Civil Engineering and Engineering Mechanics Series, Prentice Hall.
- [8] Cilenti, L., Cameron, M., Balachandran, B., 2024. Influence of noise on a rotating, softening cantilever beam. *International Journal of Non-Linear Mechanics* 159, 104582.
- [9] Clarabut, D., Robinson, B., Poirel, D., Sarkar, A., 2023. The nonlinear effects of spinning on the dynamics of a pitching cantilever. *Journal of Sound and Vibration* , 117876.
- [10] Das, S., Ray, P., Pohit, G., 2007. Free vibration analysis of a rotating beam with nonlinear spring and mass system. *Journal of Sound and Vibration* 301, 165–188.
- [11] French, A.P., 2017. *Vibrations and waves*. CRC press.
- [12] Grandgeorge, P., Baek, C., Singh, H., Johanns, P., Sano, T.G., Flynn, A., Maddocks, J.H., Reis, P.M., 2021. Mechanics of two filaments in tight orthogonal contact. *Proceedings of the National Academy of Sciences* 118, e2021684118.
- [13] Gutierrez-Prieto, E., Gomez, M., Reis, P.M., 2024. Harnessing centrifugal and euler forces for tunable buckling of a rotating elastica. *Extreme Mechanics Letters* , 102246.
- [14] Gutierrez-Prieto, E., Meulblok, C.M., van Hecke, M., Reis, P.M., 2025. Dynamic driving enables independent control of material bits for targeted memory. *arXiv preprint arXiv:2508.16257* Submitted.
- [15] Hoskoti, L., Gupta, S.S., Sucheendran, M.M., 2023. Modeling of geometrical stiffening in a rotating blade—a review. *Journal of Sound and Vibration* 548, 117526.
- [16] Inman, D., 2009. *Engineering Vibration*. Pearson Education.
- [17] Jeffcott, H.H., 1919. The lateral vibration of loaded shafts in the neighbourhood of a whirling speed: the effect of want of balance. *The London, Edinburgh, and Dublin Philosophical Magazine and Journal of Science* 37, 304–314.
- [18] Johanns, P., Grandgeorge, P., Baek, C., Sano, T.G., Maddocks, J.H., Reis, P.M., 2021. The shapes of physical trefoil knots. *Extreme Mechanics Letters* 43, 101172.
- [19] Kim, H., Chung, J., 2016. Nonlinear modeling for dynamic analysis of a rotating cantilever beam. *Nonlinear Dynamics* 86, 1981–2002.
- [20] Lacarbonara, W., Arvin, H., Bakhtiari-Nejad, F., 2012. A geometrically exact approach to the overall dynamics of elastic rotating blades—part 1: linear modal properties. *Nonlinear Dynamics* 70, 659–675.
- [21] Lo, H., Renbarger, J., 1952. Bending vibrations of a rotating beam, first us nat. Congr. Appl. Mech., Am. Soc. Mech. Eng , 75.
- [22] Meirovitch, L., 1967. *Analytical methods in vibrations*. Macmillan.
- [23] Meriam, J.L., Kraige, L.G., Bolton, J.N., 2020. *Engineering mechanics: dynamics*. John Wiley & Sons.
- [24] Piersol, A.G., Paez, T.L., 2010. *Harris’ Shock and Vibration Handbook*. 6th ed., McGraw-Hill, New York, NY.
- [25] Rajagopal, A., Mandal, D.K., 2019. A quasi-static solution for the maneuvering analysis of vehicles with rotors, in: *AIAA Scitech 2019 Forum*, p. 0863.
- [26] Rankine, W.M., 1869. On the centrifugal force of rotating shafts. *Van Nostrand’s Eclectic Engineering Magazine (1869-1879)* 1, 598.
- [27] Rao, S., 2004. *Mechanical Vibrations*. Pearson Prentice Hall.
- [28] Shigley, J., Saunders, H., Mitchell, L., 1985. *Mechanical Engineering Design*. The American Society of Mechanical Engineers (ASME).
- [29] Siddiqui, M.S., Rasheed, A., Kvamsdal, T., Tabib, M., 2017. Quasi-static & dynamic numerical modeling of full scale nrel 5mw wind turbine. *Energy Procedia* 137, 460–467.
- [30] da Silva, M.C., Hodges, D., 1986. Nonlinear flexure and torsion of rotating beams, with application to helicopter rotor blades-ii. response and stability results. *Vertica* 10, 171–186.
- [31] Southwell, R., Gough, F., 1921. The free transverse vibration of airscrew blades. *British ARC Reports and Memoranda* .
- [32] Strogatz, S.H., 2018. *Nonlinear dynamics and chaos: with applications to physics, biology, chemistry, and engineering*. CRC press.
- [33] Thomas, O., Sénéchal, A., Deü, J.F., 2016. Hardening/softening behavior and reduced order modeling of nonlinear vibrations of rotating cantilever beams. *Nonlinear dynamics* 86, 1293–1318.
- [34] Turhan, Ö., Bulut, G., 2009. On nonlinear vibrations of a rotating beam. *Journal of sound and vibration* 322, 314–335.
- [35] Van der Walt, S., Schönberger, J.L., Nunez-Iglesias, J., Boulogne, F., Warner, J.D., Yager, N., Gouillart, E., Yu, T., 2014. scikit-image: image processing in python. *PeerJ* 2, e453.
- [36] Wright, A., Smith, C., Thresher, R., Wang, J., 1982. Vibration modes of centrifugally stiffened beams. *Journal of Applied Mechanics* 49, 197–202.
- [37] Yoo, H.H., Shin, S.H., 1998. Vibration analysis of rotating cantilever beams. *Journal of Sound and Vibration* 212, 807–828.